Measurement Science and Technology

100 year anniversary
Measurement Science and Technology

PAPER

Compound fault diagnosis of rotating machinery based on adaptive maximum correlated kurtosis deconvolution and customized multiwavelet transform

To cite this article: Lianhuan Hong *et al* 2018 *Meas. Sci. Technol.* **29** 115007

IOP Publishing

Measurement Science and Technology

Meas. Sci. Technol. 29 (2018) 115007 (19pp)

https://doi.org/10.1088/1361-6501/aadefe

Compound fault diagnosis of rotating machinery based on adaptive maximum correlated kurtosis deconvolution and customized multiwavelet transform

Lianhuan Hong[1,2], **Xiaobo Liu**[1,2] **and Hongyan Zuo**[1,2]

[1] College of Mechanical and Electrical Engineering, Nanjing University of Aeronautics and Astronautics, 29 Yudao Street, Nanjing 210016, People's Republic of China

[2] School of Aeronautical Manufacturing Engineering, Nanchang Hangkong University, 696 Fenghe South Avenue, Nanchang 330063, People's Republic of China

E-mail: xbliu0791@126.com

Received 5 May 2018, revised 18 August 2018

Accepted for publication 5 September 2018

Published 4 October 2018

Abstract

Although compound fault diagnosis of rotating machinery based on vibration signals is a prominent method, it is still a challenge due to coupled fault features immersed in strong background noise. An adaptive deconvolution and denoising technology based on adaptive maximum correlated kurtosis deconvolution and multiwavelet transform is studied here. In combination with Hilbert envelope spectrum analysis, a novel compound fault diagnosis method is proposed in this paper. Based on analysis using maximum correlated kurtosis deconvolution (MCKD) theory, a parameter range estimation method is given which is favorable for MCKD parameter optimization. Flexible standard multiwavelets are used in post-processing of MCKD to enhance the denoising effect further. The minimum of a compound faults characteristic index composed of *M*-shift correlated kurtosis and square envelope spectrum entropy is adopted as the optimization criterion to set reasonable parameters for MCKD and construct customized multiwavelets using particle swarm optimization. The effectiveness of the proposed method is demonstrated by both simulated signal and practical vibration signals of a rotor test rig and an aero engine rotor experimental rig with different compound faults. The superior effectiveness and reliability of the proposed method are confirmed by comparison with other fault detection methods.

Keywords: rotating machinery, adaptive maximum correlated kurtosis deconvolution, compound fault diagnosis, customized multiwavelets

(Some figures may appear in colour only in the online journal)

1. Introduction

As a consequence of the increasing complexity of mechanical equipment, the great majority of faults emerging in rotating machinery (RM) are compound faults which will result in catastrophic accidents and huge economic losses [1]. Therefore, it is important to detect such compound faults as early as possible. Abnormal states of RM bring about symptomatic vibrations with repetitive transients, whose distinctive signature is cyclostationary and impulsive [2]. Frequency components can reveal time variant features [3], and repetitive transients can be detected from characteristic frequencies by digital spectral analysis [2]. However, the vibration signal of RM typically possesses nonlinear and nonstationary properties [4], and the coupled fault features of compound faults are immersed in heavy background noise. Therefore, it is imperative to develop appropriate deconvolution and compound fault diagnosis technology to extract the useful fault features from measured vibration signals.

To date, such methods have been proposed for compound fault diagnosis as morphological component analysis [5], demodulation algorithms [6], meshing resonance and spectral kurtosis [7], variational mode decomposition [8], blind source separation techniques [9], clustering algorithms [10, 11], empirical mode decomposition [11–13] and symplectic geometry mode decomposition [14]. However, few studies covering these methods have taken the impulsiveness and cyclostationarity into account. As a powerful time–frequency analysis technique for rotating mechanical fault diagnosis (RMFD), the multiwavelet transform (MT) has been used for deconvolution and denoising [1, 12, 13, 15–17]. However, pre-filtering is required to translate one-dimensional into multi-dimensional signals, owing to the matrix filter banks of multiwavelet systems [18], and this often destroys the orthogonality of multiwavelets or produces redundancy of the input signal [19]. Maximum correlated kurtosis deconvolution (MCKD) is an effective tool for separating out the periodic impulse faults component from the vibration signal in circumstances of intense background noise [20],and has been applied in RMFD [21, 22]. However, the main problem in the practical application of MCKD is how to set the following four parameters appropriately: the length of filter L, the number of deconvolved sequential impulses M, the maximum count of iteration N_ir and the period of interest T to obtain the best performance. Among these parameters, which will affect the validity of MCKD, T is uppermost as it is decided by sampling frequency f_s and fault characteristic frequency f_c. Only when f_s/T is approximately equal to f_c can the effectiveness of MCKD be guaranteed. To highlight the superiority of MCKD, L, M and N_ir should also be set reasonably, the prime requirement of T having been satisfied. In general, the larger L, M and N_ir, the better the performance is, but the more complex the calculation. However, if L and M are too large, the deconvolved signal will be distorted. The rigorous requirements for the parameters thus limit the application of MCKD.

To solve the above problem, we put forward a method of parameter optimization for MCKD, combine the advantages of MCKD and multiwavelets, and propose an adaptive MCKD with customized standard multiwavelet transform for the diagnosis of two-fault compound faults in rotating machinery. First, the information relating to the two faults can be crudely separated out from among the components of the original vibration using MCKD with optimized parameters twice, and used as the input signals for the MT algorithm; the preprocessing requirement of conventional MT can thus be eliminated. Second, a customized MT based on GHM multiwavelets is used as post-processing of MCKD to enhance the denoising effect further. In addition, the post-processing of traditional MT is abandoned in that the two output channels of multiwavelet coefficients correspond to the two fault component information streams. Finally, owing to the effectiveness of Hilbert transform demodulation analysis in extracting amplitude and frequency from the modulation signal [23], Hilbert transform (HT) and spectrum analysis of the denoised fault component signals are used to extract fault characteristic frequencies. The proposed method is applied to the analysis of both simulated signal and practical vibration signals with various compound faults. The results demonstrate the effectiveness of the compound fault diagnosis.

The rest of this paper is organized as follows. The summary of MCKD is reviewed in section 2. In section 3, the construction of flexible standard multiwavelets is introduced briefly. The proposed method for compound RMFD is discussed in section 4. The simulation and experimental validations are presented in section 5. Finally, conclusions are summarized in section 6.

2. Review of MCKD

Based on kurtosis, MCKD can deconvolve periodical fault signal components from raw signals. A detailed description of its excellent foundation is provided in [24]. The formula for M-shift correlated kurtosis (MCK) deconvolution of the zero-mean signal can be defined as follows:

$$\mathrm{MCK}=\frac{\sum_{n=1}^{N}\left(\prod_{m=0}^{M}y_{n-mT}\right)^2}{\left(\sum_{n=1}^{N}y_n^2\right)^{M+1}} \tag{1}$$

where y_n is given by

$$y_n=\sum_{k=1}^{L}f_k x_{n-k+1}\quad(n=1,2,\cdots,N) \tag{2}$$

(where x_n is the measured signal with sampling number of N, y_n denotes the deconvoluted signal and $\vec{f}=\begin{bmatrix}f_1 & f_2 & \cdots & f_L\end{bmatrix}'$ is a filter of length L), M is the number of deconvolved sequential impulses, and T is the period of interest and can be calculated thus:

$$T=f_s/f_c \tag{3}$$

where f_s and f_c respectively denote the sampling frequency and fault characteristic frequency.

By designing a finite impulse response (FIR) filter to maximize the MCK, the maximum MCK (MMCK) can be similarly expressed as

$$\mathrm{MMCK}=\max_{\vec{f}}\mathrm{MCK}=\max_{\vec{f}}\frac{\sum_{n=1}^{N}\left(\prod_{m=0}^{M}y_{n-mT}\right)^2}{\left(\sum_{n=1}^{N}y_n^2\right)^{M+1}}. \tag{4}$$

To find the maximum of the function, the first derivative of function (4) is set equal to zero. Thus, the nonlinear formula for $\vec{f}$ is presented as follows:

$$\vec{f}=\frac{\left\|\vec{\mathbf{y}}\right\|^2}{(M+1)\left\|\vec{\beta}\right\|^2}\left(\mathbf{X}_0\mathbf{X}_0^T\right)^{-1}\sum_{m=0}^{M}\mathbf{X}_{mT}\vec{\alpha}_m \tag{5}$$

where

$$\mathbf{X}_{r_0} = \begin{bmatrix} x_{1-r_0} & x_{2-r_0} & x_{3-r_0} & \cdots & x_{N-r_0} \\ 0 & x_{1-r_0} & x_{2-r_0} & \cdots & x_{N-r_0-1} \\ 0 & 0 & x_{1-r_0} & \cdots & x_{N-r_0-2} \\ \vdots & \vdots & \vdots & \ddots & \vdots \\ 0 & 0 & 0 & \cdots & x_{N-r_0-L+1} \end{bmatrix}_{L\times N},$$

$$\vec{\alpha}_m = \begin{bmatrix} y_{1-mT}^{-1}\left(y_1^2 y_{1-T}^2 \cdots y_{1-MT}^2\right) \\ y_{2-mT}^{-1}\left(y_2^2 y_{2-T}^2 \cdots y_{2-MT}^2\right) \\ \vdots \\ y_{N-mT}^{-1}\left(y_N^2 y_{N-T}^2 \cdots y_{N-MT}^2\right) \end{bmatrix}, \vec{\beta} = \begin{bmatrix} y_1 y_{1-T} \cdots y_{1-MT} \\ y_2 y_{2-T} \cdots y_{2-MT} \\ \vdots \\ y_N y_{N-T} \cdots y_{N-MT} \end{bmatrix}$$

$$\vec{y} = \mathbf{X}_0{}^T \vec{f}. \tag{6}$$

With the above analysis, MCK can be expressed as follows:

$$\mathrm{MCK} = \frac{\sum_{n=1}^{N}\left(\prod_{m=0}^{M}\sum_{k=1}^{L} f_k x_{n-mT-k+1}\right)^2}{\left(\sum_{n=1}^{N}\left(\sum_{k=1}^{L} f_k x_{n-k+1}\right)^2\right)^{M+1}} \quad (n = 1, 2, \cdots, N). \tag{7}$$

According to equations (5)–(7), with the given parameters L, M and T, the local optimal solution for $\vec{f}$ can be solved iteratively to separate out fault component y from x_n based on the maximum MCK criterion. The concrete steps of the iterative process have been summarized in [20]. In accordance with analyses from the literature [20, 22] and our test analysis, the maximum count of iteration N_ir also is set to 30 in this paper.

3. Multiwavelets and construction of flexible standard multiwavelets

With the multiscaling function $\Phi = [\varphi_0(t), \varphi_1(t), \cdots \varphi_{r-1}(t)]'$ and the multiwavelet function $\mathbf{\Psi} = [\psi_0(t), \psi_1(t), \cdots \psi_{r-1}(t)]'$ of multiplicity r, multiwavelets are the vector-valued composition of wavelets. The theoretical principle of multiwavelets has been described in [24]. Analogously to scalar wavelets, $\mathbf{\Phi}$ and $\mathbf{\Psi}$ satisfy the matrix dilation equations

$$\mathbf{\Phi}(t) = \sqrt{2}\sum_{k\in Z}\mathbf{H}_k\mathbf{\Phi}(2t-k) \tag{8}$$

$$\mathbf{\Psi}(t) = \sqrt{2}\sum_{k\in Z}\mathbf{G}_k\mathbf{\Phi}(2t-k). \tag{9}$$

The low-pass multifilter $\{\mathbf{H}_k \in \mathbf{R}^{r\times r}, k \in \mathbf{Z}\}$ and high-pass multifilter $\{\mathbf{G}_k \in \mathbf{R}^{r\times r}, k \in \mathbf{Z}\}$ are $r\times r$ two-scale matrices. Based on inner product principle, the effectiveness of MT lies in the degree of matching between basis functions and fault features. This means that $\mathbf{H}_k$ and $\mathbf{G}_k$ should be constructed according to fault features [25].

Owing to the impact of their properties, Geronimo–Hardin–Massopust (GHM) multiwavelets—which were constructed by Geronimo *et al* in [26]—have been widely used as common basis functions in RMFD [25]. Chui and Lian [27] recovered the GHM multiwavelet function without using fractal interpolation. According to the property of coefficients,

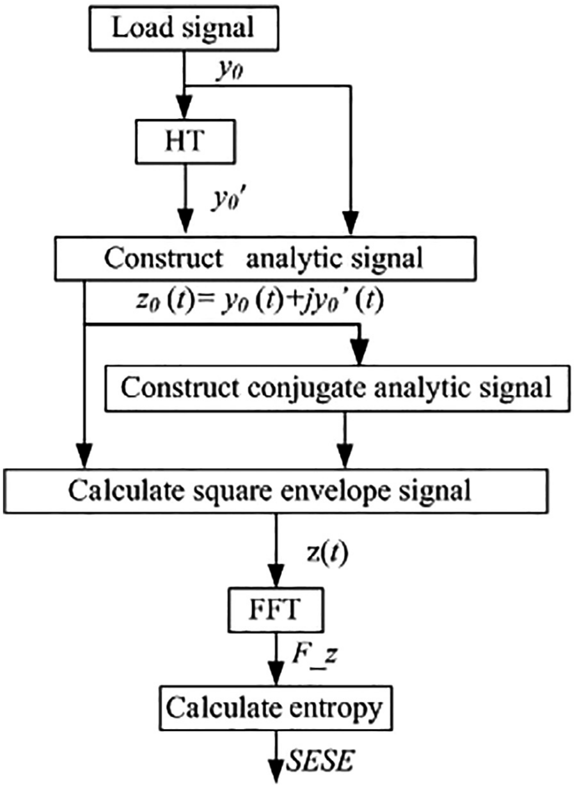

Figure 1. The algorithmic framework of SESE.

when the multiscaling functions are symmetric about 1/2 and 1, $\mathrm{supp}\varphi 1 = [0, 1]$, $\mathrm{supp}\varphi 2 = [0, 2]$, the two-scale matrix sequence can be obtained as [27]

$$H_0 = \begin{bmatrix} a_0 & b_0 \\ c_0 & d_0 \end{bmatrix}, H_1 = \begin{bmatrix} a_0 & 0 \\ c_1 & d_1 \end{bmatrix}, H_2 = \begin{bmatrix} 0 & 0 \\ c_1 & d_0 \end{bmatrix}, H_3 = \begin{bmatrix} 0 & 0 \\ c_0 & 0 \end{bmatrix}.$$

For the symmetry and orthogonality condition of multiwavelets [27], there is $b_0 = 2(c_0 + c_1)$.

Letting $a_0 = \sqrt{2}\cos\theta/2$, $b_0 = \sin\theta$, we can obtain

$$H_0 = \frac{\sqrt{2}}{2} \times \begin{bmatrix} \cos\theta & \sqrt{2}\sin\theta \\ \frac{\sqrt{2}(\sin\theta-1)}{4} & -\frac{1}{2}\cos\theta \end{bmatrix}, H_1 = \frac{\sqrt{2}}{2} \times \begin{bmatrix} \cos\theta & 0 \\ \frac{\sqrt{2}(\sin\theta+1)}{4} & 1 \end{bmatrix}$$
$$H_2 = \frac{\sqrt{2}}{2} \times \begin{bmatrix} 0 & 0 \\ \frac{\sqrt{2}(\sin\theta+1)}{4} & -\frac{1}{2}\cos\theta \end{bmatrix}, H_3 = \frac{\sqrt{2}}{2} \times \begin{bmatrix} 0 & 0 \\ \frac{\sqrt{2}(\sin\theta-1)}{4} & 0 \end{bmatrix}. \tag{10}$$

Assume the multiwavelet function $\mathbf{\Psi}(t) = [\psi_0(t), \psi_1(t)]'$, $\psi_0(t)$ is symmetric about 1 and $\psi_1(t)$ is antisymmetric about 1, we can obtain

$$G_0 = \frac{\sqrt{2}}{2} \times \begin{bmatrix} \frac{\sqrt{2}(\sin\theta-1)}{4} & -\frac{1}{2}\cos\theta \\ \frac{-(\sin\theta-1)}{2} & -\frac{\sqrt{2}}{2}\cos\theta \end{bmatrix}, G_1 = \frac{\sqrt{2}}{2} \times \begin{bmatrix} \frac{\sqrt{2}(\sin\theta+1)}{4} & -1 \\ \frac{-(\sin\theta+1)}{2} & 0 \end{bmatrix}$$
$$G_2 = \frac{\sqrt{2}}{2} \times \begin{bmatrix} \frac{\sqrt{2}(\sin\theta+1)}{4} & -\frac{1}{2}\cos\theta \\ \frac{(\sin\theta+1)}{2} & -\frac{\sqrt{2}}{2}\cos\theta \end{bmatrix}, G_3 = \frac{\sqrt{2}}{2} \times \begin{bmatrix} \frac{\sqrt{2}(\sin\theta-1)}{4} & 0 \\ \frac{(\sin\theta-1)}{2} & 0 \end{bmatrix} \tag{11}$$

where θ is a free parameter. When $\theta = \arccos(0.6)$, this is a GHM multiwavelet. Thus, by equations (10) and (11), the flexible standard multiwavelet library can be established for the subsequent fault diagnosis.

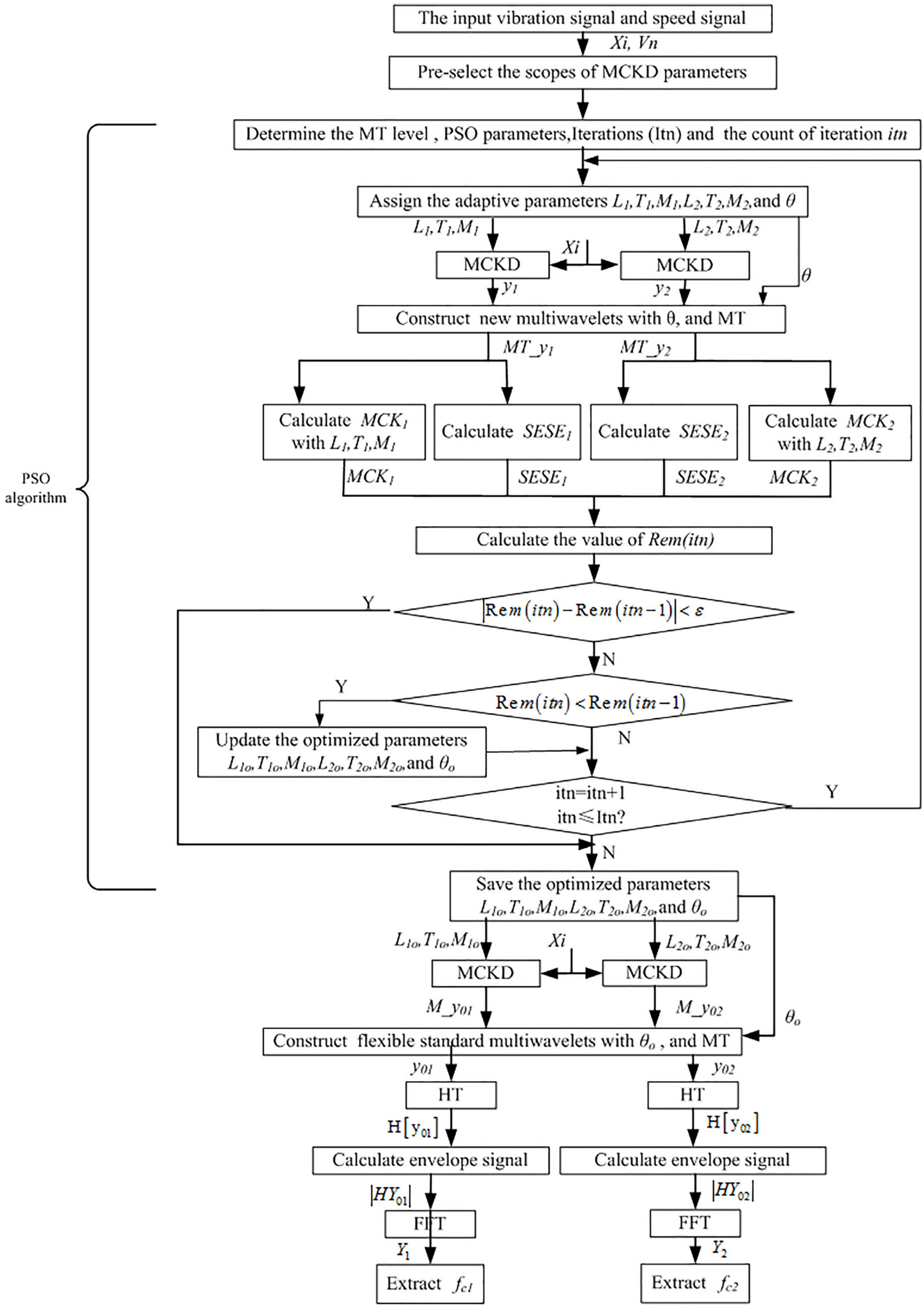

Figure 2. Flow chart of the proposed method.

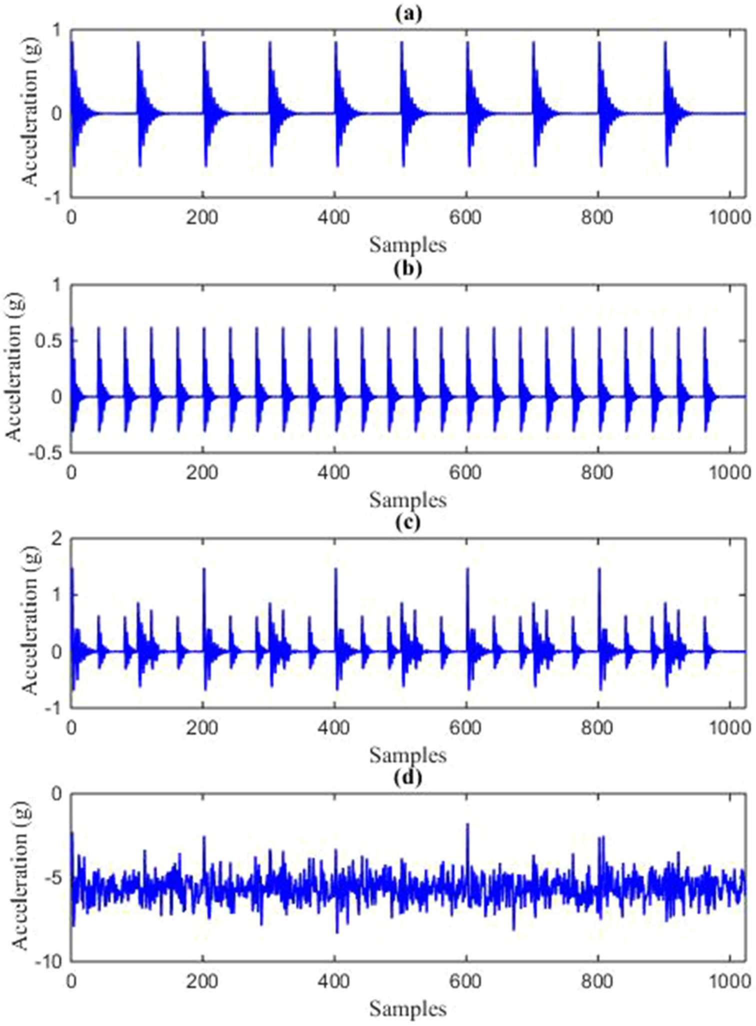

Figure 3. (a) Impulse signal $A_1(t)$ with the frequency of 10 Hz; (b) impulse signal $A_2(t)$ with the frequency of 25 Hz; (c) $A_{12}(t) = A_1(t) + A_2(t)$; (d) the simulated signal $A_0(t)$.

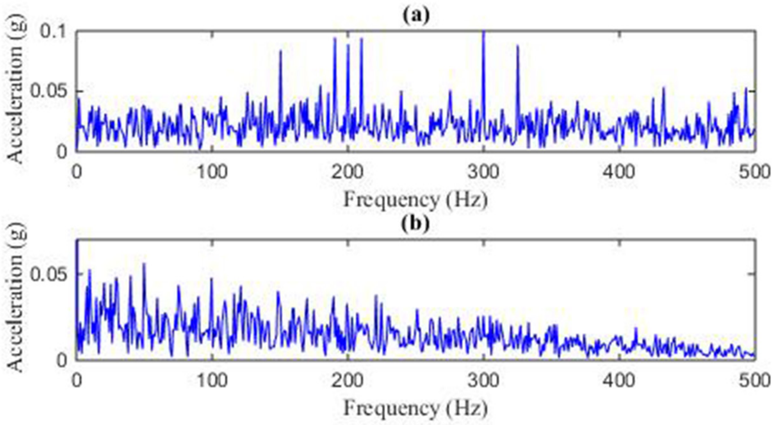

Figure 4. (a) FFT spectrum of $A_0(t)$ and (b) the directly Hilbert envelope spectrum of $A_0(t)$.

4. The proposed method for compound fault diagnosis

In reading this paper, it should be noted that the proposed method focuses on extracting the major fault characteristic frequency (MFCF) of different faults from the analyzed signal; therefore, certain minor components accompanied by faults are ignored. The proposed method is composed of five major steps: (1) pre-select the scope of the MCKD parameters; (2) select the optimal parameters of the proposed method using the optimization algorithm; (3) decouple the fault information signals from the input vibration signal according to the

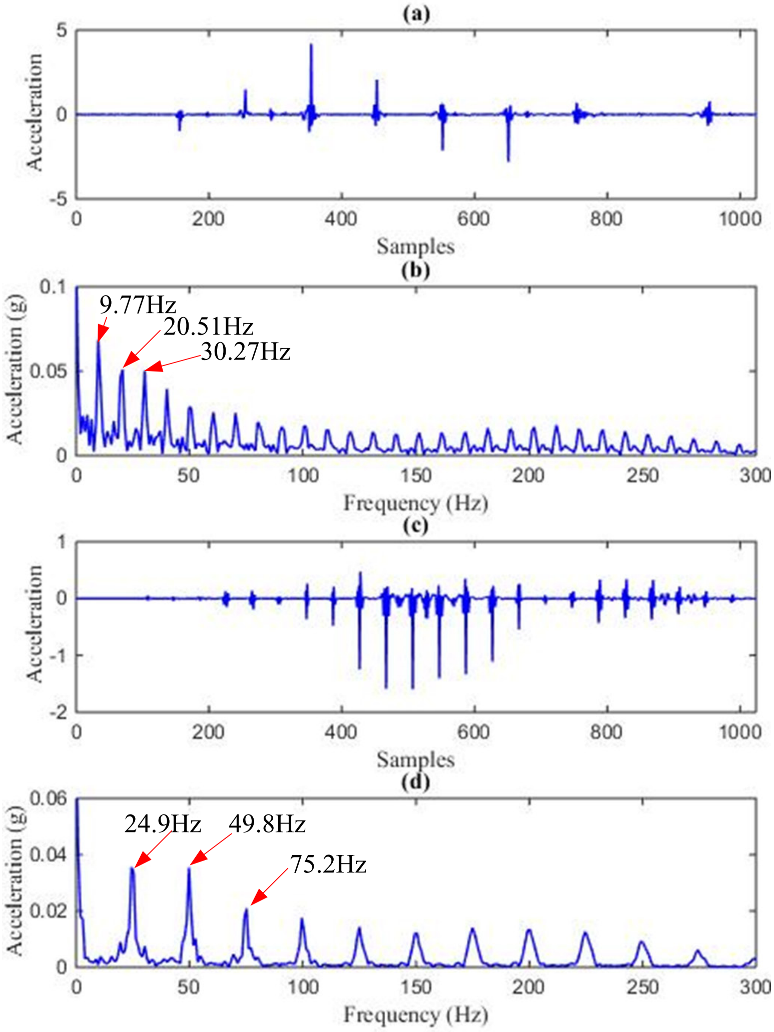

Figure 5. Results for case 1 using the proposed method: (a) time domain waveform of one extracted signal; (b) Hilbert envelope spectrum of (a); (c) time domain waveform of another extracted signal; (d) Hilbert envelope spectrum of (c).

optimal parameters using MCKD; (4) de-noise the decoupled signals using the flexible standard multiwavelet transform; (5) extract MFCF through envelope spectrum based on HT and envelope analysis.

4.1. Pre-selecting the scopes of MCKD parameters

In this paper, particle swarm optimization (PSO), which is a typical evolutionary computation method and can achieve the best or near best solution of certain problems [28], is applied to the adaptive setting of the optimal parameters for the proposed method. It is necessary to pre-select the scope of MCKD parameters to achieve the fastest possible PSO.

Vibration magnitude varies significantly at the fault characteristic frequency when a fault occurs. For example, when the speed is higher than the first-order critical speed, components at (1/3–1/2) $\times$ operating frequency f_o may be sensitive to slight partial rub. Strong $2 \times f_o$ and $1 \times f_o$ harmonic frequency components will be sensitive to shaft misalignment faults and mass unbalance defects respectively [29, 30]. For pre-selection of the scope, we can set $f_{c\alpha} \approx \alpha \times 0.5 \times f_o$ (here, $\alpha = 1, 2, \ldots, N_1$) and the corresponding period of interest can be estimated as follows:

$$T_\alpha = \text{round}\left(f_s/f_{c\alpha}\right) = \text{round}\left(2f_s/\alpha \times f_o\right). \tag{12}$$

Within one sampling period, if there are $f_s/20f_o$ periods at the operating frequency of RM, then $\alpha f_s/40f_o$ for a fault. Here, 20 is the resampling factor [20]. So, the number of deconvolved sequential impulses can be estimated as follows:

$$M_\alpha = \text{ceil}\left(\frac{f_s/20}{f_o} \times \frac{f_{c\alpha}}{f_o}\right) - 1 = \text{ceil}\left(\frac{\alpha f_s}{40 f_o}\right) - 1. \tag{13}$$

In order to meet the requirement of $L > 2f_s/f_o$ [22] and equation (3), set $L = \text{round}(2.5T_\alpha)$. The general procedure of the pre-selection of the scope for T and M is as follows:

Step 1. Calculate $f_o = V_n/60$, where V_n is the input speed signal.
Step 2. Calculate T_α, M_α from equations (12) and (13).
Step 3. Calculate MCK(α, β) based on L, M_α and $T(\alpha, \beta) = \text{round}((\beta * 0.05 + 0.75) \times T_\alpha)$, β is varied between 1 and 9 at a step of 1, α is varied between 1 and 8 at a step of 1.
Step 4. Calculate $\text{CK}(\alpha) = \sum_\beta \text{MCK}(\alpha, \beta)$, and take the corresponding α of the maximum CK(α) as fault factor αm_1.

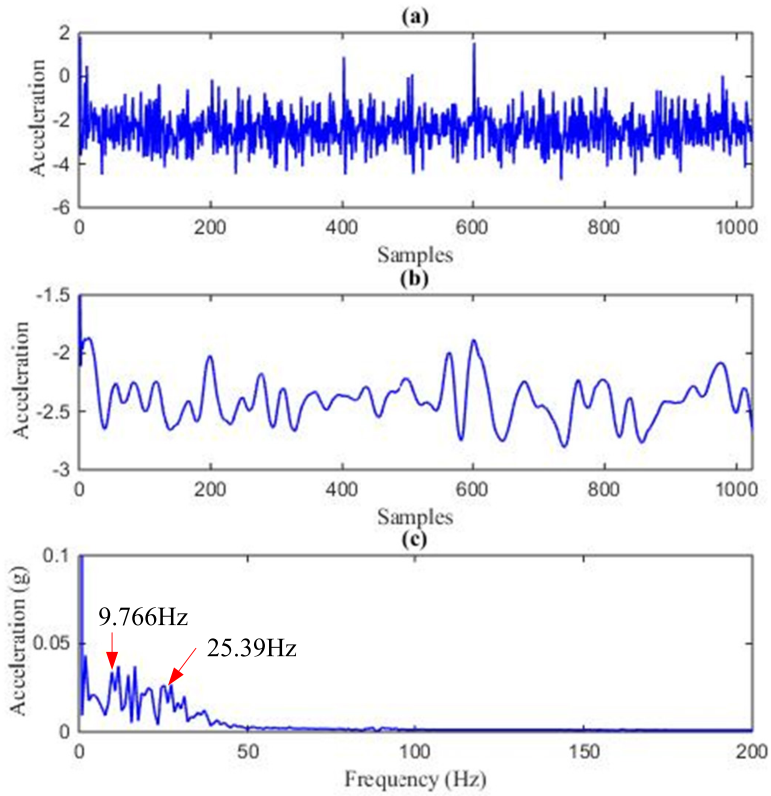

Figure 6. Results for case 1 using the Db6-HT method: (a) the simulated signal $A_0(t)$; (b) time domain waveform by Db6 wavelet transform; (c) Hilbert envelope spectrum of (b).

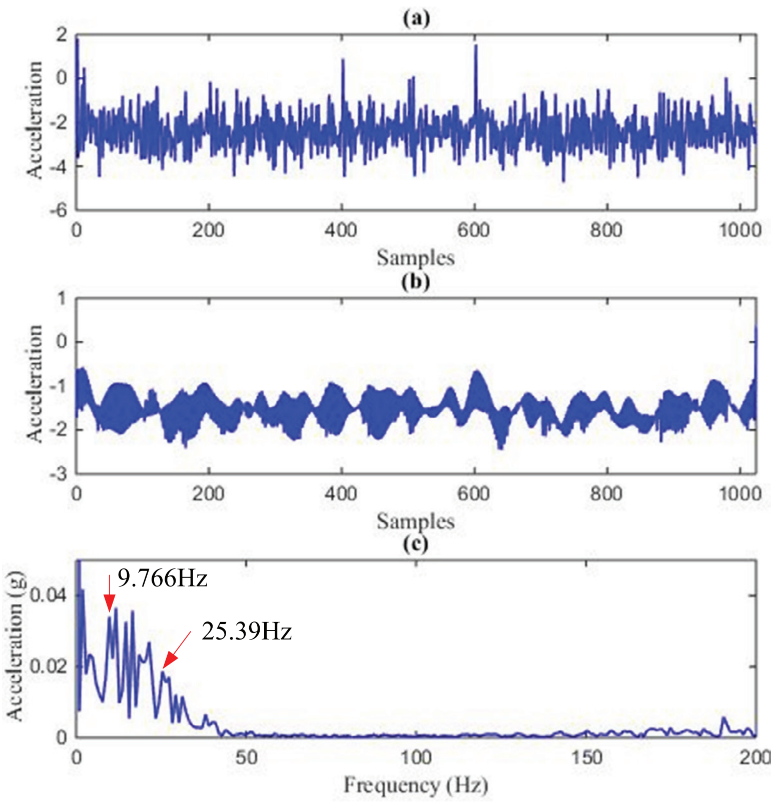

Figure 7. Results for case 1 using the GHM-HT method: (a) the simulated signal $A_0(t)$; (b) time domain waveform by GHM multiwavelet transform; (c) Hilbert envelope spectrum of (b).

Table 1. Performance indexes of the results analyzed by two methods.

Method	One extracted signal			Another extracted signal			Rem
	Kur	MCK	EE	Kur	MCK	EE	
IMCK-HT	20.7809	0.039	6.5444	5.7512	0.0075	6.6026	26.7821
Proposed method	163.9982	0.1283	5.3029	87.0714	0.1351	5.7753	11.2248

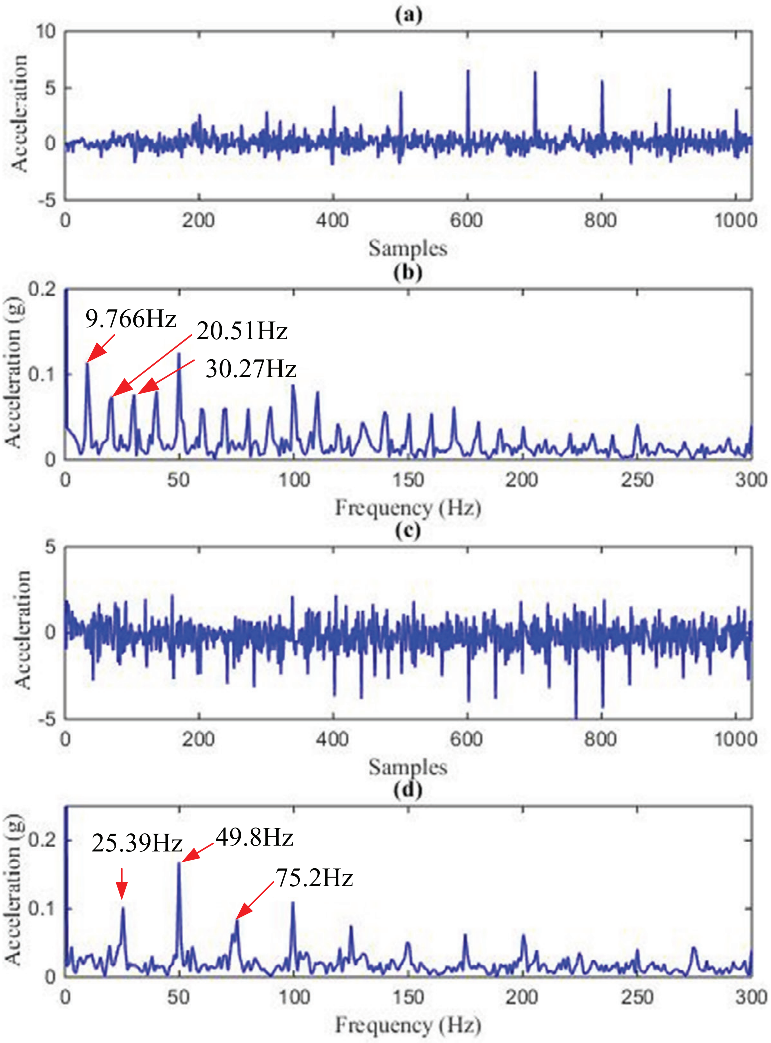

Figure 8. Results for case 1 using the IMCKD-HT method: (a) time domain waveform of one extracted signal; (b) Hilbert envelope spectrum of (a); (c) time domain waveform of another extracted signal; (d) Hilbert envelope spectrum of (c).

Step 5. Set the scope $[0.8T_{\alpha m1}, 1.2T_{\alpha m1}]$ for T, $[2, M_{\alpha m1}+1]$ for M and $[2.5T_{\alpha m1}, 5T_{\alpha m1}]$ for L.

It is also necessary to take the second largest CK(α) and fault factor αm_2 to extract another fault component information, and set the scopes $[0.8T_{\alpha m2}, 1.2T_{\alpha m2}]$, $[2, M_{\alpha m2}+1]$ and $[2.5T_{\alpha m2}, 5T_{\alpha m2}]$.

4.2. Optimization criterion for the selection of parameters

To ensure the effectiveness of the proposed method in extracting the fault features from the vibration signal, a compound fault characteristic index composed of MCK and square envelope spectrum entropy (SESE) is used as the evaluation criterion, being of benefit in selecting the MCKD parameters and constructing the flexible standard multiwavelets. Thereinto, MCK can reveal the periodic impulsiveness of the analysis results in the time domain [20]; according to MCKD theory: the larger the MCK, the more evident will be the continuous periodical nature of the decoupled signal in the time domain. SESE can indicate cyclostationarity in the frequency domain [2]; on the basis of information theory: the smaller the SESE, the more obvious will be the periodic impact feature and the higher the signal-to-noise ratio (SNR). Thus, the composite index is more effective than any simple one.

Analysis and calculation of MCK have been introduced in section 2. Here, SESE will be expatiated.

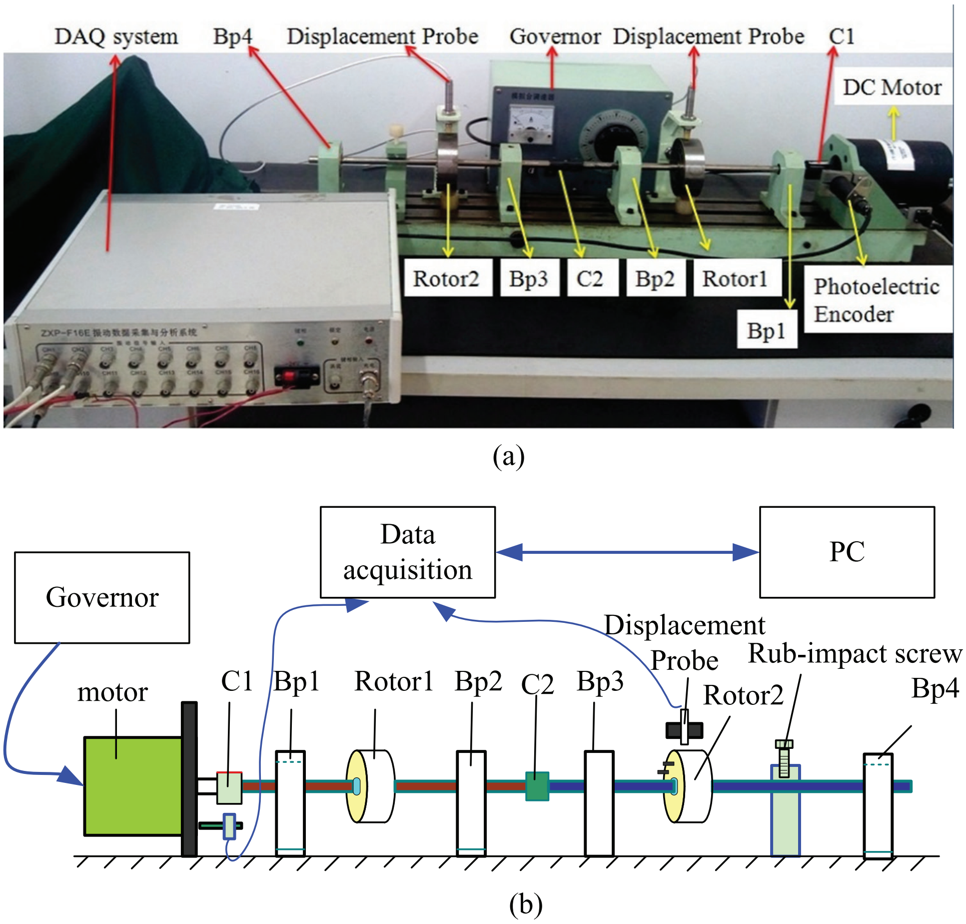

Figure 9. Rotor test-bed and test system. (a) Photograph of the rotor test-bed and test system. (b) Structural schematic of the geometry.

4.2.1. Calculation principle and process of SESE. The algorithmic framework of SESE is presented in figure 1.

The procedure for calculating SESE of the signal $y_0(t)$ can be described as follows:

Step 1. Transform $y_0(t)$ by HT to get the quadrature signal:

$$y_0'(t) = H[y_0(t)] = \frac{1}{\pi}\int_{-\infty}^{+\infty}\frac{y_0(t)}{t-\tau}\mathrm{d}\tau.$$

Step 2. Construct the analytic signal: $z_0(t) = y_0(t) + \mathrm{j}y_0'(t)$.
Step 3. Construct the conjugate analytic signal: $z_0'(t) = y_0(t) - \mathrm{j}y_0'(t)$.
Step 4. Calculate the square envelope signal: $z(t) = z_0(t)\,z_0'(t)$.
Step 5. Calculate the square envelope spectrum by fast Fourier transform (FFT):

$$F\_z = |\mathrm{FFT}(z(t))|.$$

Step 6. Calculate SESE:

$$\mathrm{SESE} = -\sum_{i=1}^{K_Z}\mathrm{PFZ}(i)\lg\mathrm{PFZ}(i) \tag{14}$$

where $\mathrm{PFZ}(i) = \frac{F\_z(i)}{\sum_{i=1}^{K_Z}F\_z(i)}, \quad K_Z = \mathrm{length}(F\_z).$

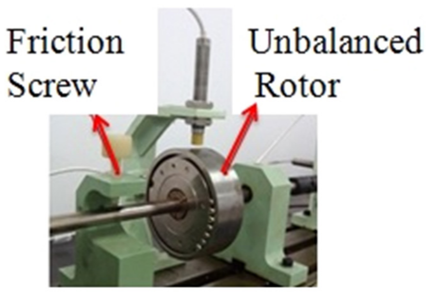

Figure 10. Components of imbalance and rubbing impact faults.

4.2.2. Compound fault characteristic index. In general, MCK is less than 1 and SESE has large errors—of several orders of magnitude—in the early stages of failure. In order to take advantage of both MCK and SESE as far as possible, the compound faults characteristic index is defined as follows:

$$\mathrm{Rem} = \frac{\sum_{ix=1}^{n_1}\mathrm{Rem}_{ix}}{n_1} = \frac{\sum_{ix=1}^{n_1}(\mathrm{SESE}_{ix}\times|\lg(\mathrm{MCK}_{ix})|)}{n_1} \tag{15}$$

where n_1 is the total number of fault types, and MCK_{ix} and SESE_{ix} for the ixth fault component are given by equations (7) and (14) respectively. The minimum Rem and PSO are taken as the optimization object and a tool, respectively, to seek the optimal two sets of L, M, T and θ for the proposed method. In this paper, θ is sought within the interval $[-\pi, \pi]$, the initial

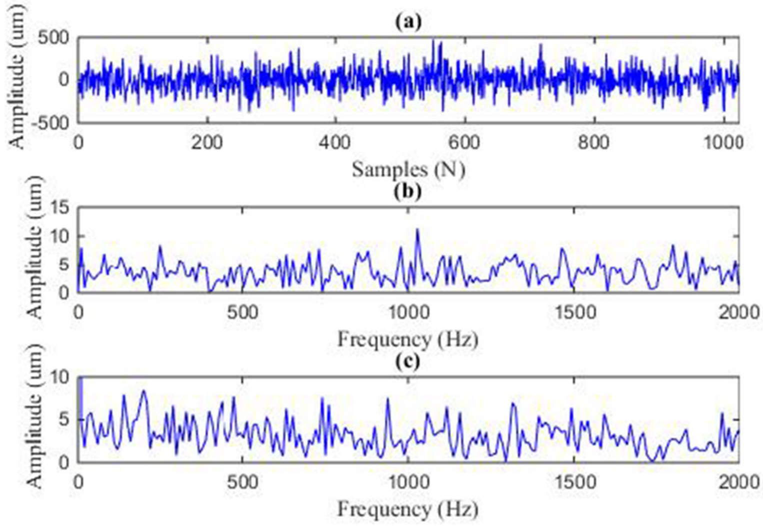

Figure 11. Initial vibration signal in case 2: (a) the measured vibration signal; (b) the frequency spectrum of (a); (c) the direct Hilbert envelope spectrum of (a).

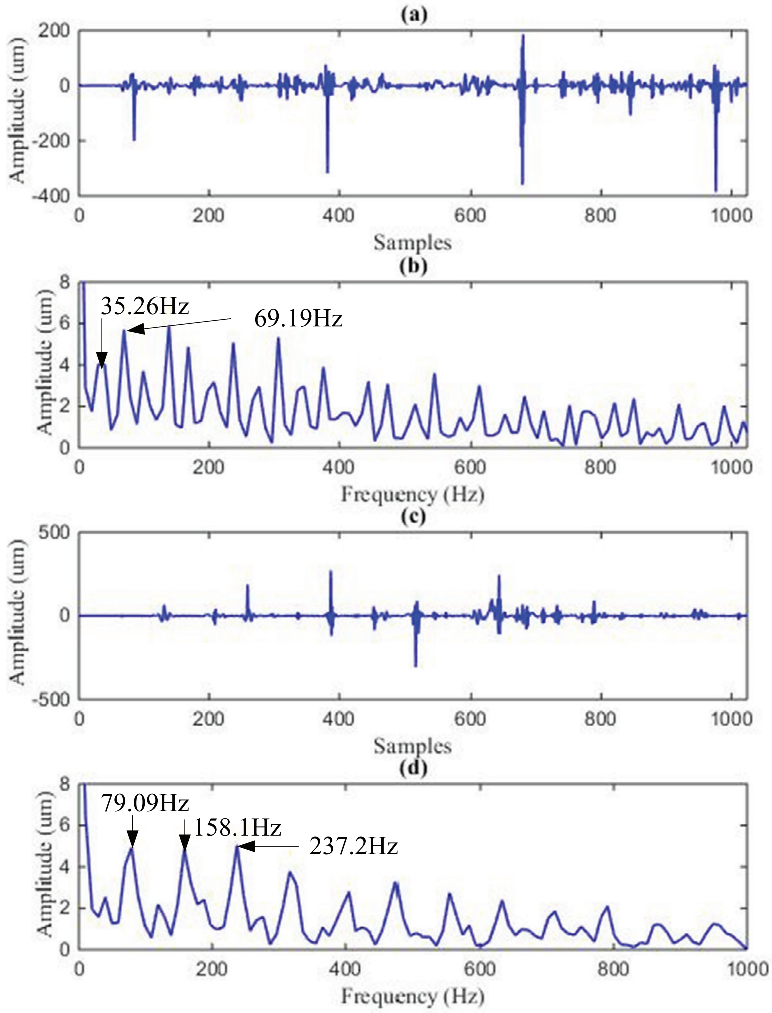

Figure 12. Results for case 2 using the proposed method: (a) time domain waveform of fault component I, (b) Hilbert envelope spectrum of (a) and (c) time domain waveform of fault component II and (d) Hilbert envelope spectrum of (c).

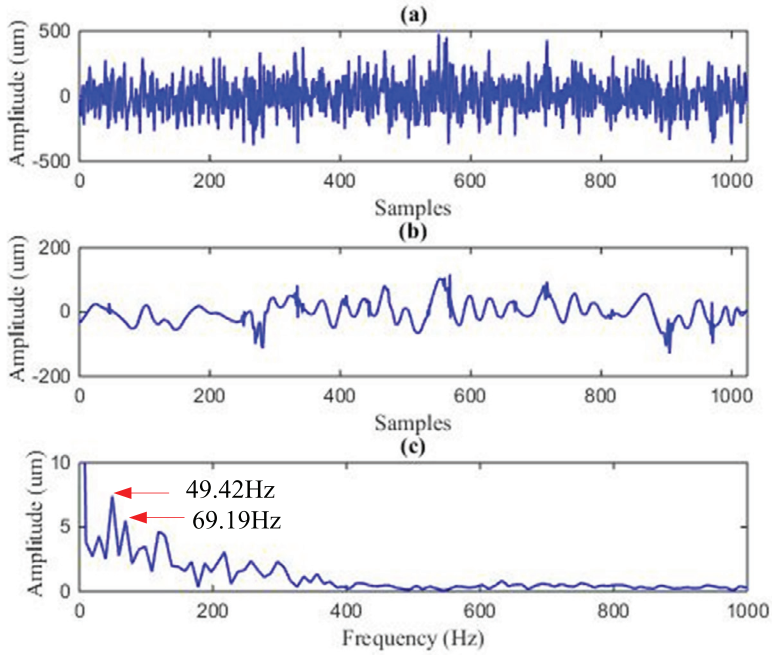

Figure 13. Results for case 2 using the Db6-HT method: (a) the measured vibration signal; (b) time domain waveform by Db6 wavelet transform; (c) Hilbert envelope spectrum of (b).

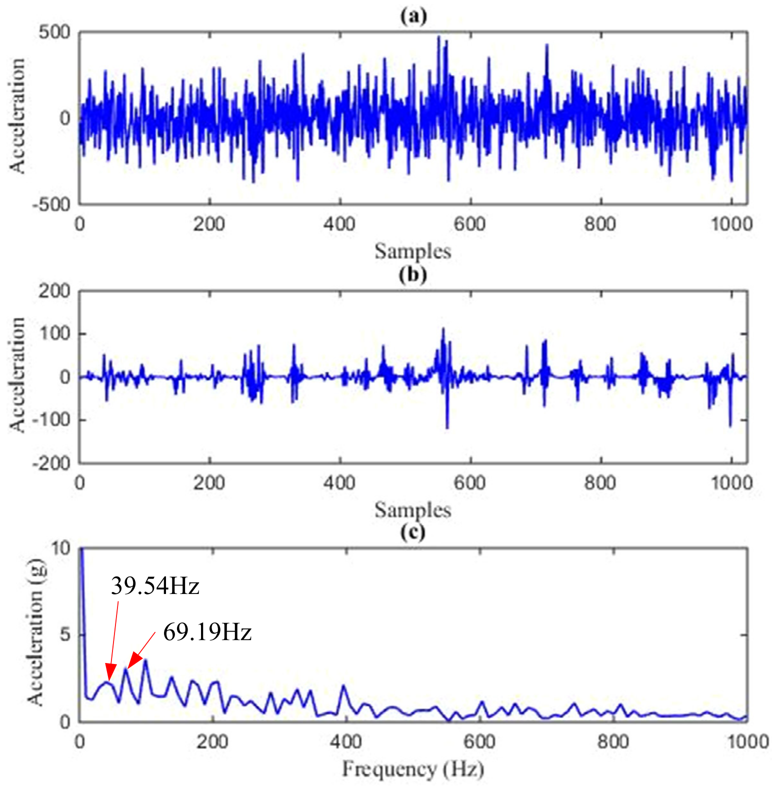

Figure 14. Results for case 2 using the GHM-HT method: (a) the measured vibration signal; (b) time domain waveform by GHM multiwavelet transform; (c) Hilbert envelope spectrum of (b).

scopes of MCKD parameters T, M and L can be set in terms of processes described in section 4.1. The parameters of the PSO algorithm are set as follows: the number of particles is set to 40, the maximum count of iteration to 100, the constant inertia weight to 0.8 and the learning factors to 2.05.

4.3. Procedure of compound fault diagnosis

The detailed procedure of the proposed method is presented as a flow chart in figure 2. Meanwhile, the steps of the method can be described as follows:

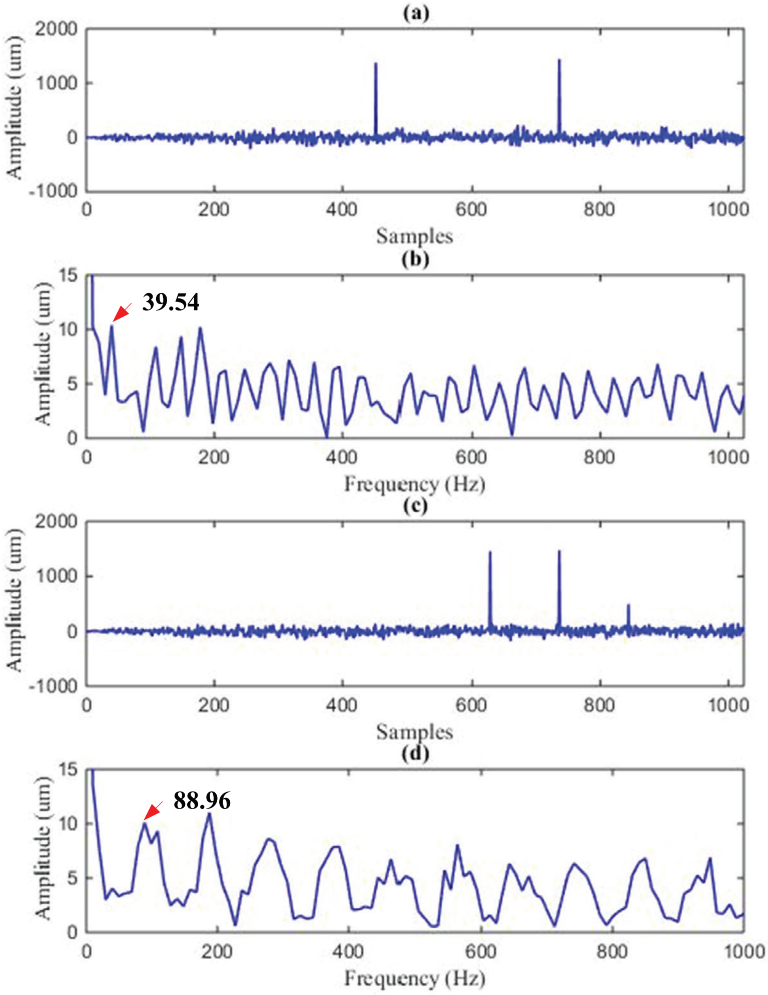

Figure 15. Results for case 2 using the AMCKD-HT method: (a) time domain waveform of fault component I; (b) Hilbert envelope spectrum of (a); (c) time domain waveform of fault component II; (d) Hilbert envelope spectrum of (c).

Step 1. Input the acquired vibration signal X_i and the speed signal V_n.

Step 2. Pre-select the scope of MCKD parameters based on section 4.1.

Step 3. Set the multiwavelet decomposition level, PSO parameters and the count of iteration itn = 1.

Step 4. Assign adaptive parameters: L_1, M_1, T_1, L_2, M_2, T_2 and θ, then extract two informations y_1, y_2 from X_i using MCKD twice.

Step 5. Construct the new multiwavelets of θ based on equations (10) and (11), and obtain the denoised signals MT_y_1 and MT_y_2 by adopting MT for y_1 and y_2.

Step 6. Calculate Rem(itn) by equation (15). If $\text{Rem(itn)} < \text{Rem(itn} - 1)$, then update the optimized parameters L_{1o}, T_{1o}, M_{1o}, L_{2o}, T_{2o}, M_{2o} and θ_o. Repeat the process from Step 4 until the maximum count of iteration is reached or $|\text{Rem (itn)} - \text{Rem (itn} - 1)| < \varepsilon$ is satisfied (here, ε is an infinitesimal positive tolerance level).

Step 7. Roughly extract two fault information components M_y_{01}, M_y_{02} from X_i using MCKD twice with [L_{1o}, T_{1o}, M_{1o}] and [L_{2o}, T_{2o}, M_{2o}] respectively.

Step 8. Construct the flexible standard multiwavelets of θ_0 based on equations (10) and (11), obtain the denoised fault information components y_{01} and y_{02} using the MT.

Step 9. Extract the fault feature frequency from the envelope spectrum calculated using HT and FFT.

5. Application of the proposed method

To validate the effectiveness of the proposed method in extracting major fault characteristic components embedded in heavy noise, three experimental cases have been implemented in this section. It has been proven that the improved MCKD (IMCKD) presented in [22] is more efficient than MCKD as proposed in [20]. Having similar properties to adaptive multiwavelets, the Daubechies 6 wavelet (Db6) has been widely used as a common wavelet transform basis function for RMFD [25]. Meanwhile, GHM multiwavelets with fixed base functions are widely used in practice [1, 25]. Traditionally, the most commonly used frequency analysis

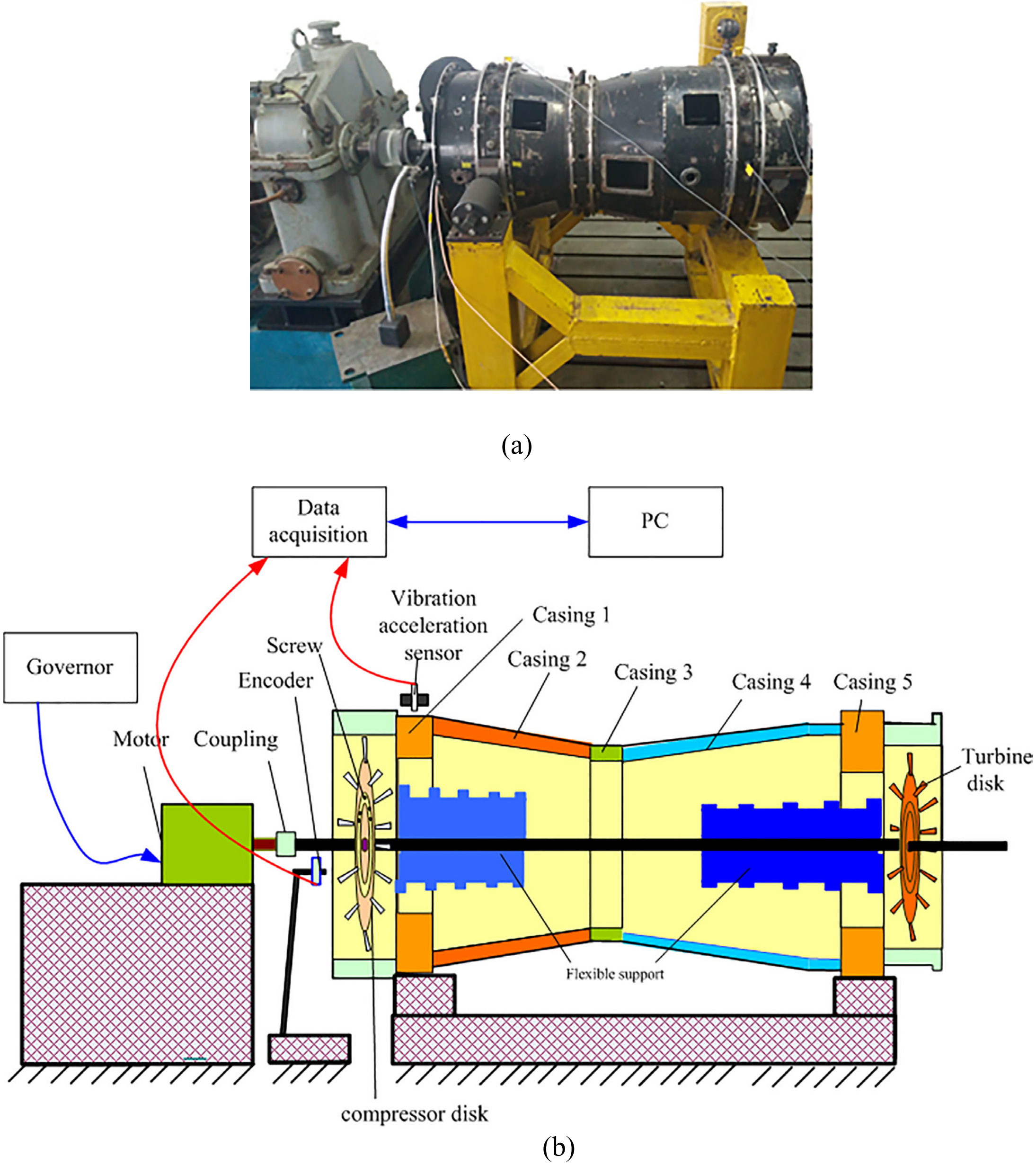

Figure 16. Aero-engine rotor experimental rig: (a) photograph; (b) structural schematic. Part (a) reprinted from [31], Copyright 2015, with permission from Elsevier.

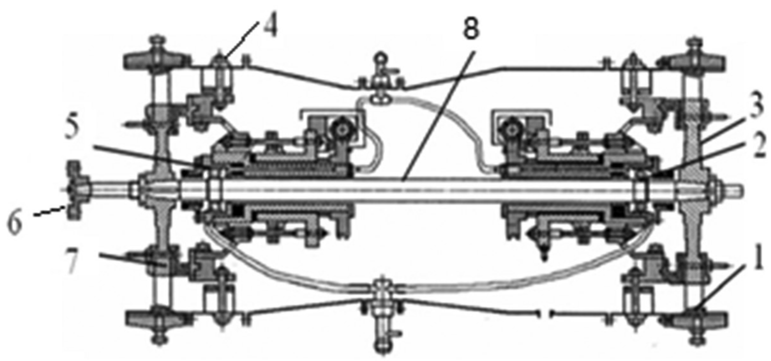

Figure 17. Structural sketch of the aero-engine rotor experimental rig. 1—rubbing ring, 2—ball bearing, 3—turbine disk, 4—casing test point, 5—roller bearing, 6—coupling, 7—compressor disk, 8—shaft. Reprinted from [31], Copyright 2015, with permission from Elsevier.

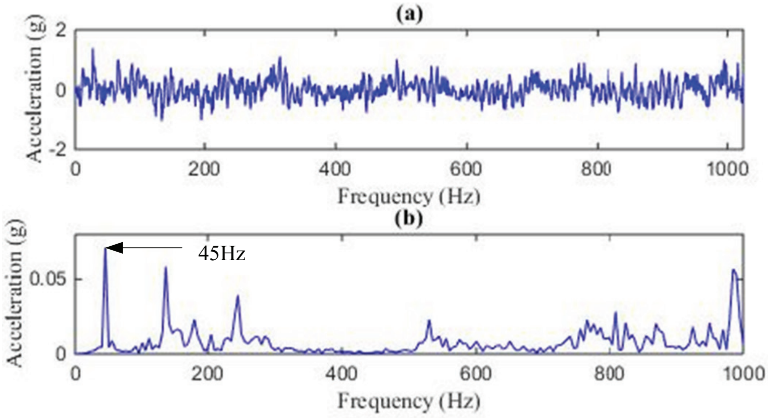

Figure 18. Vibration signal under normal conditions: (a) time domain waveform of the vibration signal; (b) frequency spectrum of (a).

method is FFT. Envelope analysis based on HT is another popular method of extracting periodic features [1]. To confirm the efficiency of the proposed method, it is compared with FFT, HT envelope analysis, GHM transforms with Hilbert envelope spectrum (GHM-HT), Db 6 transforms with Hilbert envelope spectrum (Db6-HT), IMCKD with Hilbert envelope spectrum (IMCKD -HT).

5.1. Case 1: simulated signal experiment

In this paper, a simulation experiment is designed and implemented firstly. In order to simulate the actual case of compound faults of RM, the simulation experiment is designed as follows. Two impulse signals are described: $A_1\,(t) = -\mathrm{e}^{-100t}\sin(800\pi t)$, displayed in figure 3(a) and $A_2\,(t) = -0.8\mathrm{e}^{-200t}\sin(600\pi t)$, displayed in figure 3(b). The signal $A_{12}(t)$ displayed in figure 3(c) comprises the periodic impulses $A_1(t)$ and $A_2(t)$, with periods of 0.1 s and 0.04 s respectively. The sampling frequency is 1000 Hz. White Gaussian noise with the signal-to-noise ratio per sample of -3.2 dB and random noise are added to $A_{12}(t)$ and form the simulated signal $A_0(t)$ shown in figure 3(d). The features of periodic impulses can hardly be found in figure 3(d) for the heavy noise.

The frequencies 10 Hz and 25 Hz (for impulse signals A_1 and A_2 respectively) are hardly visible in the FFT spectrum of $A_0(t)$, as shown in figure 4(a). The Hilbert envelope spectrum of $A_0(t)$ is shown in figure 4(b). It is also hard to discern the corresponding frequency components clearly.

In order to validate the effectiveness of the proposed method, adaptable deconvolution and denoising techniques are applied to extract the periodic features from $A_0(t)$. The optimal adaptive parameters L_1, M_1, T_1, L_2, M_2, T_2 and θ are determined at [285, 8, 98, 130, 7, 40 and arccos(0.6316)] by the process in section 4. The analyzed result using the proposed method is presented in figure 5. It is notable that the impulse components can be seen clearly in figures 5(a) and (c). From figures 5(b) and (d), harmonic components $1X$–$3X$ of the characteristic frequencies of 10 Hz and 25 Hz are notably apparent. The results indicate that the proposed method can successfully identify and extract features from a simulated signal composed of two simultaneous impulse signals.

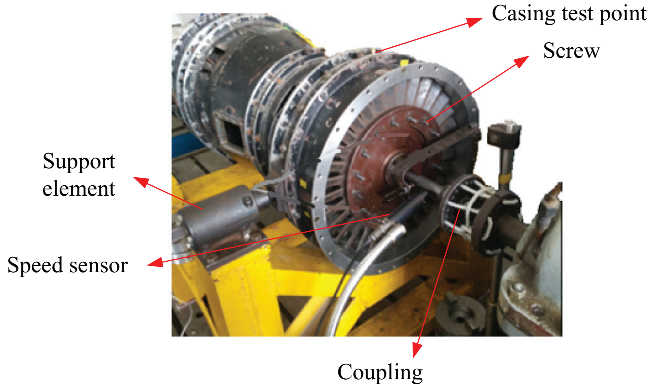

Figure 19. Components of imbalance and misalignment fault. Reprinted from [31], Copyright 2015, with permission from Elsevier.

The results of the same simulated signal analyzed by using Db6-HT, GHM-HT and IMCKD-HT, are illustrated in figures 6–8 respectively. As illustrated in figures 6 and 7, the Db6-HT and GHM-HT methods can get rid of high frequency noise effectively. However, the two characteristic frequencies of 10 Hz and 25 Hz in the low frequency segment are not obvious.

When L_1, M_1, T_1, L_2, M_2, and T_2 are determined at [200, 1, 100, 80, 1 and 40] according to [22], the IMCKD-HT method can also extract the two characteristic frequencies. The performance indexes, which include kurtosis (Kur), envelope entropy (EE), MCK and compound fault characteristic index (Rem), analyzed by IMCK-HT and the proposed method are calculated; results are shown in table 1. Compared with the other methods, the proposed method is more effective.

5.2. Case 2: application to a rotor test rig

5.2.1. The rotor test rig. A rotor test rig, depicted in figure 9, is used as the test equipment in this section. The test rig is a fundamental model of a dual-rotor system. The rig has a 9.5 mm diameter semi-flexible coupling (C2) connecting alloy shaft 1 (320 mm in length) and shaft 2 (200 mm in length). Shaft 1 is connected to a DC shunt motor (rating current is 2.5 A and power output is 250 W) by a rigid coupling (C1). Two sliding bearings of 45 steel (76 mm in diameter and 25 mm thick), acting as balancing rotors, are mounted to each shaft. The rotating

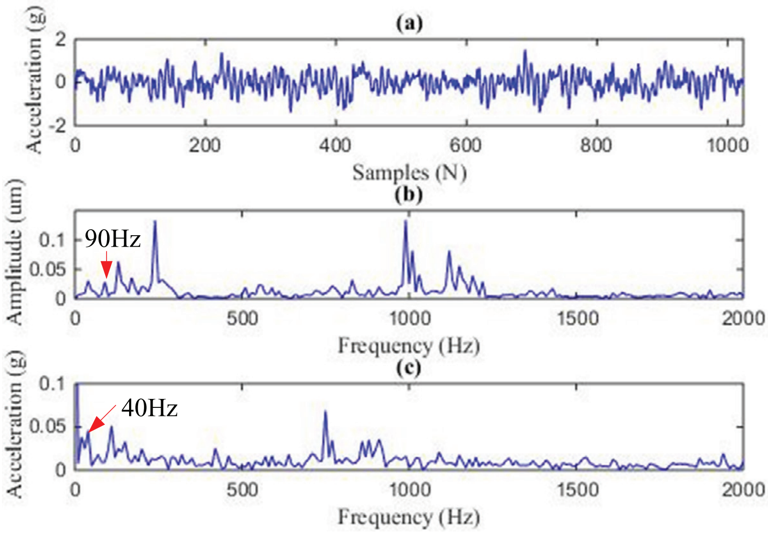

Figure 20. Measured vibration signal for case 3: (a) time domain waveform of the raw vibration signal; (b) frequency spectrum of (a); (c) direct Hilbert envelope spectrum of (a).

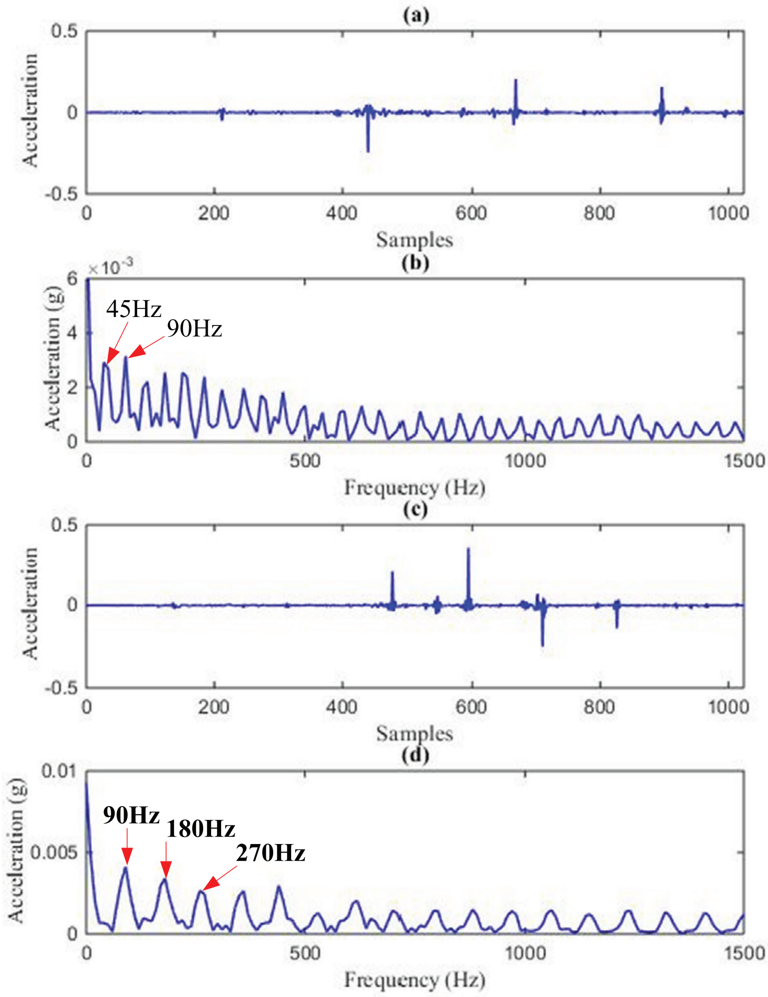

Figure 21. Results for case 3 using the proposed method: (a) time domain waveform of the misalignment fault component; (b) Hilbert envelope spectrum of (a); (c) time domain waveform of the imbalance fault component; (d) Hilbert envelope spectrum of (c).

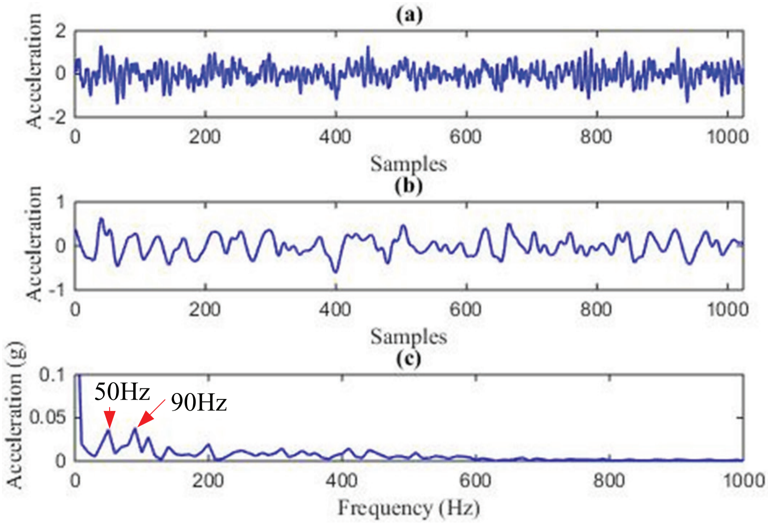

Figure 22. Results for case 3 using the Db6-HT method: (a) the measured vibration signal; (b) time domain waveform by Db6 wavelet transform; (c) Hilbert envelope spectrum of (b).

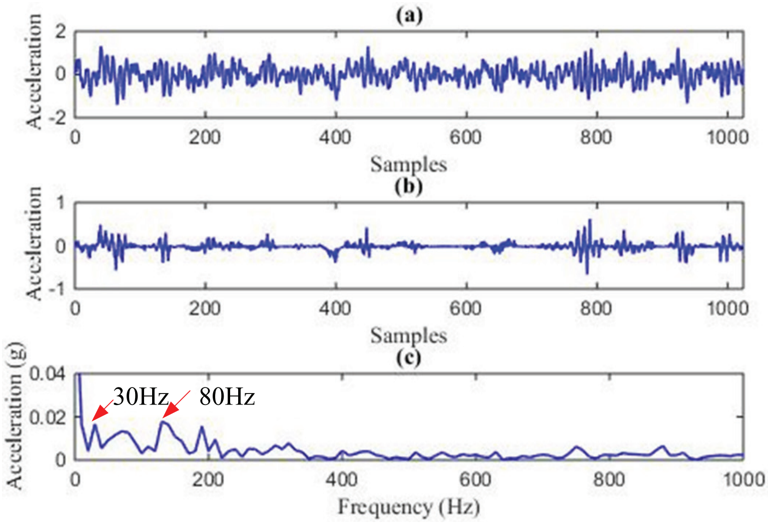

Figure 23. Results for case 3 using the GHM-HT method: (a) the measured vibration signal; (b) time domain waveform by GHM multiwavelet transform; (c) Hilbert envelope spectrum of (b).

assembly is supported by four oil-lubricated 9.5 mm internal diameter plain bearing pedestals (Bp1–Bp4). Each bearing pedestal is fixed to the rig's foundation with two M5 inner hexangular set screws. Two industrial eddy current displacement probes (sensitivity is 8 V mm^{-1}) are used to measure the radial vibration displacements of the rotor 1 and rotor 2. The vibration signals of the rotors are transmitted to a 16 bit, 24 channel analogue-to-digital converter, which is a crucial part of the data acquisition (DAQ) system. Excitation voltage and armature current are supplied to the DC motor by a governor. The speed signal measured by photoelectric encoder based on the keyway phase measuring principle is transmitted to the DAQ system, connected to a personal computer via a USB cable. Vibration and speed data are recorded and stored on the personal computer for subsequent processing and analysis.

5.2.2. Experiments conducted. An experimental device generating compound faults consisting of imbalance fault and impact fault was constructed according to the following procedure, as shown in figure 10. Seven 0.3 g M2 × 10 mm screws are installed on the circumferential groove at 33 mm from the centre of the rotor 2. The added screws will lead to unbalancing of rotor 2 and thus to an imbalance fault in the rotor test rig. Furthermore, a friction screw is mounted on a bracket is fixed to the rig's foundation by screws, close to rotor 2. Rubbing will occur between this friction screw and shaft 2 when the clearance between them is too small. When the rig is run with the unbalanced rotor, the friction screw is adjusted slowly in a clockwise direction until shaft 2 shows a slight friction trace. At this point, a compound fault case comprising a rubbing impact fault (Fault I) and imbalance fault (Fault II) is established. Experiments were conducted at a speed of 4744 r min^{-1} with the sampling frequency $f_s = 10.21$ kHz. According to the diagnostics of the rotor test rig, the major fault characteristic frequencies of rubbing impact and imbalance faults were $f_{c1} = 34.59$ Hz and $f_{c2} = 79.07$ Hz respectively.

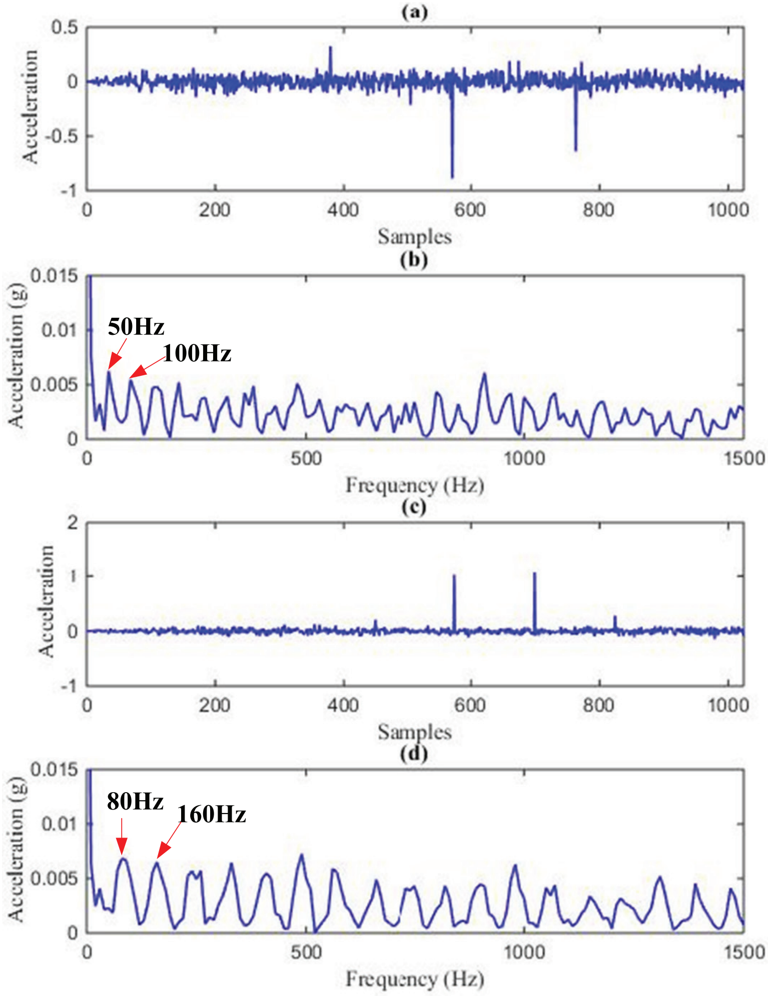

Figure 24. Results for case 3 using the IMCKD-HT method: (a) time domain waveform of fault component I; (b) Hilbert envelope spectrum of (a); (c) time domain waveform of fault component II; (d) Hilbert envelope spectrum of (c).

5.2.3. Characteristic frequency extraction based on the proposed method. An experimental vibration signal of length 1024 is illustrated in figure 11(a); there are no useful features to be seen in the time domain waveform. The frequency spectrum of the vibration signal found by applying FFT is displayed in figure 11(b). Figure 11(c) shows the Hilbert envelope spectrum. As can be seen in figure 11, the periodic impulses related to the compound faults are submerged in the environmental noise. In other words, the information necessary to diagnose the failures is not clear in the frequency spectrum or the Hilbert envelope spectrum.

To identify and extract features of the compound faults effectively, the proposed method is applied in the analysis of the vibration signal. The optimal adaptive parameters L_1, M_1, T_1, L_2, M_2, T_2 and θ are determined at [137, 2, 297, 121, 4, 128 and arccos(0.6152)] by the process in section 4. The result of this analysis is presented in figure 12. The de-noised fault component signals with obvious impact characteristics found by the proposed method are shown in figures 12(a) and (c). The low frequency portion of the Hilbert envelope spectrums are plotted in figures 12(b) and (d). In figures 12(b) and (d), the $1X$–$2X$ harmonic components of the characteristic frequencies of 34.59 Hz and 79.07 Hz are notably apparent, indicating the simultaneous presence of rubbing impact and imbalance faults. The results show that the proposed method can successfully extract the corresponding fault characteristic frequencies from the vibration signal due to a compound fault.

To highlight the effectiveness of the proposed method, the same test signal is analyzed using the Db6-HT method, GHM-HT method and IMCKD-HT method. The results of analysis using the above methods are illustrated in figures 13–15. Compared with the proposed method, none of the methods mentioned above has the capability to extract the characteristic frequencies of rubbing impact and imbalance faults from the measured vibration signal.

5.3. Case 3: application to aero engine rotor experimental rig

5.3.1. Introduction of the experimental setup. A photograph and structural sketch of the experimental setup used in this section are shown in figures 16 and 17 [31, 32]. The unit is composed of a motor, gearbox, coupling, ball bearing, turbine disk, roller bearing, compressor disk, and so on. A detailed description of the experimental setup has been presented in [31].

A test vibration signal displayed in figure 18(a) was taken at the sampling frequency of 10 240 Hz and the rotational speed of 2682 r $\min^{-1}$ (calculate $f_o = 2682/60 = 44.7$ Hz) under normal conditions. The frequency spectrum of the signal is shown in figure 18(b). Although there is some noise, the frequency of 45 Hz, which almost equals the fundamental frequency of 44.7 Hz, is clear in the low frequency range.

5.3.2. Experiments conducted. An experimental device with compound faults consisting of imbalance fault and coupling misalignment was established according to the following procedure, as shown in figure 19 [32]. An accelerometer is mounted on the casing test point. An imbalance fault is set by fitting new nuts onto the screws, as shown in figure 19. A shaft misalignment, in which the input shaft of the experimental rig and the output shaft of the motor do not share an identical centerline, is set by adjusting a support element installed on the bench to change the position of the experimental setup.

The measured vibration signal displayed in figure 20(a) is sampled at a sampling frequency of 10 240 Hz and rotational speed of 2678 r $\min^{-1}$ (here, $f_o = 2678/60 = 44.63$ Hz). Since strong $1 \times f_o$ harmonic frequency component is sensitive to mass imbalance defects [30] and $2 \times f_o$ is sensitive to shaft misalignment faults [29], the major characteristic frequencies of misalignment and imbalance fault can be calculated as 89.26 Hz (approximately equal to 90 Hz) and 44.63 Hz (approximately equal to 45 Hz) respectively. The frequency spectrum and Hilbert envelope spectrum of the vibration are shown in figures 20(b) and (c). Only the frequency of 90 Hz, which is approximately double the rotational frequency, can be seen faintly in figure 20(b).

5.3.3. Characteristic frequency extraction based on the proposed method. The proposed method is introduced to analyze the measured vibration signal and extract the major fault characteristic frequencies of compound faults. Figure 21 presents the analyzed results. Here, the optimal adaptive parameters L_1, M_1, T_1, L_2, M_2, T_2 and θ are determined at [124, 2, 239, 193, 3, 116 and arccos(0.6171)] by the process in section 4, the compound faults characteristic index is 11.1271. It can be seen from figure 21(a) and (c), strong periodic impulses are revealed clearly. Low frequency portion of the Hilbert envelope spectrums are plotted in figures 21(b) and (d). From figure 21(b), the MFCF of imbalance fault 90 Hz (approximately equal to 89.26 Hz) and the doubling frequency 180 Hz can be observed clearly. Moreover, the MFCF of misalignment fault 45 Hz (approximately equal to 44.63 Hz) and the doubling frequency 90 Hz are also clear in figure 21(d).

Finally, the same signal is processed by other methods. In none of the results from figures 22–24 can the two MFCF and the doubling frequencies be found simultaneously.

6. Conclusions

Based on MCKD and the multiwavelet transform, the adaptive deconvolution and denoising technology can overcome the weaknesses of each and take full advantage of both. To set reasonable MCKD parameters more efficiently, the scopes of the parameters should be calculated before PSO optimization. Meanwhile, flexible standard multiwavelets are constructed to enhance the denoising effect further. In combination with the Hilbert envelope spectrum, a novel compound fault diagnosis method is proposed in this paper. The experimental tests on the simulated signal, rotor test rig and aero engine rotor rig with two faults have been implemented and presented to validate the effectiveness of the proposed approach.

Some findings need to be mentioned according to the experimental results. First, the results demonstrate that the effectiveness of MCKD is mainly determined by the period of interest T. Because T could not be set accurately, MFCF cannot be extracted exactly using the IMCKD-HT method in cases 2 and 3. Although dependence on accurate setting of the MCKD parameters can be reduced by the use of flexible standard multiwavelets in post-processing, the essential step in the proposed method is the setting of T. It is thus necessary to develop a better method by which to set T accurately, to highlight the superiority of MCKD in the future. Second, the proposed method for extracting MFCF did not work on all the compound fault diagnoses. The variety of fault features brings a great deal of difficulty and challenge to fault diagnosis. The MFCF of the same fault can change with the working speed or fault degree. Morever, when a subordinate component of one fault is more obvious than the major component of another fault, the subordinate characteristic frequency can be mistaken for the other MFCF.

Last but not least, due to the complexity of machinery configuration and the multiplicity of faults, a single vibration signal cannot reach the required standards of reliability and accuracy. Multi-sensor data fusion technology is becoming a research hotspot for fault diagnosis. So, more efficient data processing methods for compound fault diagnosis based on multiple vibration signals should be developed in the future.

Acknowledgments

This work was supported by the National Natural Science Foundation of China (Grant no. 51365040) and Natural Science Fund of Jiangxi Province (Grant no. 20151BAB206060).

Special thanks should be expressed to G L McDonald for providing the MCKD algorithm.

The authors would like to sincerely thank all the anonymous reviewers for the valuable comments that greatly helped to improve the manuscript.

ORCID iDs

Lianhuan Hong https://orcid.org/0000-0002-7268-7767

References

[1] Chen J, Zi Y, He Z and Yuan J 2013 Compound faults detection of rotating machinery using improved adaptive

redundant lifting multiwavelet *Mech. Syst. Signal Process.* **38** 36–54
[2] Antoni J 2016 The infogram: entropic evidence of the signature of repetitive transients *Mech. Syst. Signal Process.* **74** 73–94
[3] Feng Z, Liang M and Chu F 2013 Recent advances in time-frequency analysis methods for machinery fault diagnosis: a review with application examples *Mech. Syst. Signal Process.* **38** 165–205
[4] Chen J, Li Z, Pan J, Chen G, Zi Y, Yuan J, Chen B and He Z 2016 Wavelet transform based on inner product in fault diagnosis of rotating machinery: a review *Mech. Syst. Signal Process.* **70–71** 1–35
[5] Yu D, Wang M and Cheng X 2016 A method for the compound fault diagnosis of gearboxes based on morphological component analysis *Measurement* **9** 519–31
[6] Zhao D, Li J, Cheng W and Wen W 2016 Compound faults detection of rolling element bearing based on the generalized demodulation algorithm under time-varying rotational speed *J. Sound Vib.* **378** 109–23
[7] Wang T, Chu F, Han Q and Kong Y 2017 Compound faults detection in gearbox via meshing resonance and spectral kurtosis methods *J. Sound Vib.* **392** 367–81
[8] Li Z, Chen J, Zi Y and Pan J 2017 Independence-oriented VMD to identify fault feature for wheel set bearing fault diagnosis of high speed locomotive *Mech. Syst. Signal Process.* **85** 512–29
[9] Li Z, Yan X, Tian Z, Yuan C, Peng Z and Li L 2013 Blind vibration component separation and nonlinear feature extraction applied to the nonstationary vibration signals for the gearbox multi-fault diagnosis *Measurement* **46** 259–71
[10] Du J, Wang S and Zhang H 2013 Layered clustering multi-fault diagnosis for hydraulic piston pump *Mech. Syst. Signal Process.* **36** 487–504
[11] Asr M Y, Ettefagh M M, Hassannejad R and Razavi S N 2017 Diagnosis of combined faults in rotary machinery by non-naive bayesian approach *Mech. Syst. Signal Process.* **85** 56–70
[12] Jiang H, Li C and Li H 2013 An improved EEMD with multiwavelet packet for rotating machinery multi-fault diagnosis *Mech. Syst. Signal Process.* **36** 225–39
[13] Zhang X and Zhou J 2013 Multi-fault diagnosis for rolling element bearings based on ensemble empirical mode decomposition and optimized support vector machines *Mech. Syst. Signal Process.* **41** 127–40
[14] Pan H, Yang Y, Li X, Zheng J and Cheng J 2019 Symplectic geometry mode decomposition and its application to rotating machinery compound fault diagnosis *Mech. Syst. Signal Process.* **114** 189–211
[15] He S, Chen J, Zhou Z, Zi Y and Wang Y 2016 Multifractal entropy based adaptive multiwavelet construction and its application for mechanical compound-fault diagnosis *Mech. Syst. Signal Process.* **76–7** 742–58
[16] Chen J, Wan Z, Pan J, Zi Y, Wang Y, Chen B, Sun H, Yuan J and He Z 2016 Customized maximal-overlap multiwavelet denoising with data-driven group threshold for condition monitoring of rolling mill drivetrain *Mech. Syst. Signal Process.* **68–9** 44–67
[17] Chen J, Zi Y, He Z and Wang X 2012 Construction of adaptive redundant multiwavelet packet and its application to compound faults detection of rotating machinery *Sci. China Technol. Sci.* **55** 2083–90
[18] Geronimo J, Hardin D, Suter B and Xia X 1996 Why and how prefiltering for discrete multiwavelet transforms C *ICASSP: 1996 IEEE Int. Conf. on Acoustics, Speech, and Signal Processing* (*Atlanta, GA*) pp 1578–81
[19] Lebrun J and Vetterli M 1998 Balanced multiwavelets theory and design *IEEE Trans. Signal Process.* **4** 1119–25
[20] McDonald G L, Zhao Q and Zuo M J 2012 Maximum correlated kurtosis deconvolution and application on gear tooth chip fault detection *Mech. Syst. Signal Process.* **33** 237–55
[21] Jia F, Lei Y, Shan H and Lin J 2015 Early fault diagnosis of bearings using an improved spectral kurtosis by maximum correlated kurtosis deconvolution *Sensors* **15** 29363–77
[22] Miao Y, Zhao M, Lin J and Lei Y 2017 Application of an improved maximum correlated kurtosis deconvolution method for fault diagnosis of rolling element bearings *Mech. Syst. Signal Process.* **92** 173–95
[23] Feldman M 2011 Hilbert transform in vibration analysis *Mech. Syst. Signal Process.* **25** 735–802
[24] Strela V 1996 Multiwavelets: theory and applications *PhD Thesis* Massachusetts Institute of Technology, United States
[25] Yuan J, He Z, Zi Y, Lei Y and Li Z 2009 Adaptive multiwavelets via two-scale similarity transforms for rotating machinery fault diagnosis *Mech. Syst. Signal Process.* **23** 1490–508
[26] Geronimo J S and Hardin D P 1994 Fractal functions and wavelet expansions based on several scaling functions *J. Approx. Theory* **3** 373–401
[27] Chui C K and Lian J 1996 A study of orthonormal multi-wavelets *Appl. Numer. Math.* **20** 273–98
[28] Shirkhani R, Jazayeri-Rad H and Hashemi S J 2014 Modeling of a solid oxide fuel cell power plant using an ensemble of neural networks based on a combination of the adaptive particle swarm optimization and Levenberg–Marquardt algorithms *J. Nat. Gas Sci. Eng.* **21** 1171–83
[29] Chandra Sekhar Reddy M and Sekhar A S 2015 Detection and monitoring of coupling misalignment in rotors using torque measurements *Measurement* **61** 111–22
[30] Bendjama H, Bouhouche S and Boucherit M S 2012 Application of wavelet transform for fault diagnosis in rotating machinery *Int. J. Mach. Learn. Comput.* **2** 82–7
[31] Chen G 2015 Vibration modelling and verifications for whole aero-engine *J. Sound Vib.* **349** 163–76
[32] Chen G 2017 DES-NUAA (http://ides.nuaa.edu.cn)